INORGANIC CHEMISTRY
FRONTIERS

RESEARCH ARTICLE

View Article Online
View Journal | View Issue

Cite this: *Inorg. Chem. Front.*, 2023, **10**, 2030

Melilite oxychalcogenide $Sr_2FeGe_2OS_6$: a phase-matching IR nonlinear optical material realized by isomorphous substitution†

He-Di Yang,‡[a,b,c] Sheng-Hua Zhou,‡[a,b,d] Mao-Yin Ran,[a,b,d] Xin-Tao Wu,[a,b,d] Hua Lin *[a,b,d] and Qi-Long Zhu *[a,b,d]

Transition-metal-based chalcogenides have recently emerged as greatly promising infrared nonlinear optical (IR-NLO) candidates due to their unique structural chemistries and rich optical properties. However, Fe-based IR-NLO chalcogenides with phase-matching (PM) features have not yet been reported. In this work, a new non-centrosymmetric (NCS) melilite oxychalcogenide, $Sr_2FeGe_2OS_6$, has been prepared by an isomorphous substitution method, and the relationships between the microscopic crystal structure and macroscopic NLO activity were systematically investigated. $Sr_2FeGe_2OS_6$ adopts the tetragonal space group of $P\bar{4}21m$ (no. 113) and features a unique two-dimensional structure with Cairo pentagonal tiling layers formed by the alternating connection of $[Ge_2OS_6]$ dimers and $[FeS_4]$ tetrahedra *via* corner-sharing and with the charge-balanced Sr^{2+} cations between these layers. Excitingly, $Sr_2FeGe_2OS_6$ is the first Fe-based example capable of achieving PM in the IR-NLO chalcogenide system and displays an outstanding IR-NLO comprehensive performance, including a wide energy gap (E_g = 2.24 eV), sufficient second-harmonic-generation (SHG) efficiency (d_{eff} = 5.89 pm V^{-1} at 2050 nm) and strong laser-induced damage threshold (LIDT = 14.42 MW cm^{-2}). Deeper structural and theoretical analysis suggests that the ordered arrangement of NLO-active motifs, $[Ge_2OS_6]$ dimers and $[FeS_4]$ tetrahedra, makes significant contributions to the strong d_{eff} and large birefringence (Δn). This work not only demonstrates a PM Fe-based NCS material for the first time but also puts forward a new design avenue for high-performance IR-NLO materials.

Received 24th December 2022,
Accepted 18th February 2023

DOI: 10.1039/d2qi02733j

rsc.li/frontiers-inorganic

Introduction

Nonlinear optical (NLO) technology plays an increasingly important role in materials analysis, high-resolution imaging, laser communication and other scientific research studies.[1–5] In addition, pulse lasers, optical modulators and optical memory based on NLO technology are generally applied in today's industrial society and life.[6,7] The existing commercial inorganic infrared (IR) NLO crystals $AgGaS_2$, $AgGaSe_2$, and $ZnGeP_2$ cannot meet the increasing market demand because of their inherent defects of low laser-induced damage threshold (LIDT), non-phase-matching (NPM) behaviour and two-photon absorption, respectively.[8–10] Therefore, it is crucial to design and synthesize new compounds that can combine non-centrosymmetric (NCS) structures and excellent comprehensive characteristics.

Transition-metal (TM) elements show a variety of physical and chemical properties due to their unique electronic structures, which hold a place of importance in the NLO field.[11–14] To date, more than 500 TM-based IR-NLO materials have been reported, which show extraordinary advantages as potential powerful candidates. First, benefiting from the second-order Jahn–Teller effect, they can reduce the energy barrier and then form a variety of coordination modes. Second, three common $[TMQ_2]$, $[TMQ_3]$ and $[TMQ_4]$ basic building units (BBUs) in this system not only exist independently, but can also combine with others to form one-dimensional (1D) chains, two-dimensional (2D) layers and three-dimensional (3D) frameworks. Third, they have low melting points and good physical and chemical stabilities, indicating the easy availability of large-

[a]*State Key Laboratory of Structural Chemistry, Fujian Institute of Research on the Structure of Matter, Chinese Academy of Sciences, Fuzhou, Fujian 350002, China. E-mail: linhua@fjirsm.ac.cn, qlzhu@fjirsm.ac.cn*
[b]*Fujian Science & Technology Innovation Laboratory for Optoelectronic Information of China, Fuzhou 350002, China*
[c]*College of Chemistry, Fuzhou University, Fujian 350002, China*
[d]*University of the Chinese Academy of Sciences, Beijing 100049, China*

†Electronic supplementary information (ESI) available: Additional experimental and theory results, together with additional tables and figures. CCDC 2227377. For ESI and crystallographic data in CIF or other electronic format see DOI: https://doi.org/10.1039/d2qi02733j

‡These authors contributed equally to this work.

size crystals. At present, promising TM-based IR-NLO materials are mainly based on the d^{10} elements, while other d-orbit TM-centered products are relatively few, especially Fe-based materials.[15–17] More than one thousand Fe-based NCS compounds of various types have been reported in the past century, for example, chalcogenides (*e.g.*, $FeMo_2S_4$,[18] $Cu_{1.068}Fe_{1.068}S_2$ [19]), oxides (*e.g.*, $FeGaO_3$,[20] $BiFeO_3$ [21]), phosphides (*e.g.*, $LaFe_xCo_{2-x}P_2$,[22] $An_2Fe_{12}P_7$ (An = U, Th)[23]), halides (*e.g.*, $Na_2Fe_2F_7$,[24] $LiMnFeF_6$ [25]), and oxyhalides (*e.g.*, $CaFeO_2Cl$,[26] $KFe(C_2O_4)F$ [27]). However, two- or multi-photon absorption is a frequent occurrence because of their narrow band gaps (E_g < 2.0 eV),[28,29] so most of them have been excluded from the NLO field.

In 2010, Li's group synthesized the first NLO-active ferroborate crystal, $K_2Fe_2B_2O_7$ (space group $P321$ (no. 150)),[30] which possesses [FeO_4] and [BO_3] BBUs in its 2D layered structure and displays weak second harmonic generation (SHG) efficiency (d_{eff} = 0.4 × KDP). In 2019, Mei's group reported a germanium-based sulfide, $Ba_6Cu_2FeGe_4S_{16}$ (space group $I\bar{4}3d$ (no. 220)).[31] Its 3D structure is composed of [GeS_4] and [$Ge(Cu/Fe)_3S_{13}$] units and a [BaS_8] dodecahedron and has an E_g of 1.72 eV and a d_{eff} of 1.5 × $AgGaSe_2$. Then, Wang's group discovered a quaternary $K_2FeGe_3S_8$,[32] which adopts the space group of $P2_1$ (no. 4), constructed from 1D [$FeGeS_4$] chains connected by [Ge_2S_4] units. $K_2FeGe_3S_8$ exhibits a large E_g (2.1 eV) and a small d_{eff} (0.25 × $AgGaS_2$). Recently, Cu_2FeSiS_4 with antiferromagnetic and weak SHG susceptibility has been reported by Tan's group,[33] which crystallizes in $Pmn2_1$ (no. 31) and displays a wurtzite structure composed of hexagonally close packed S and inserted metal ions. Unfortunately, all of these show normal dispersion $n(2w) > n(w)$, indicating NPM behaviour.[34] Generally, a NPM nature dramatically decreases their ultimate NLO output efficiency and hinders their practical applications. For IR-NLO materials, phase-matching (PM) is a critical factor to realize applications in IR lasers and is beneficial for increasing energy conversion efficiency.[35–39]

As hotspots of recent research, oxychalcogenides have demonstrated that the structural evolution from a single anion unit to a heteroanionic unit can enhance anisotropy and achieve a good balance between wide E_g and sufficiently large d_{eff}.[40–43] Among them, melilite, $AE_2MM'_2OS_6$ (where M and M′ represent a variety of metal elements in divalent to tetravalent states), has attracted considerable attention owing to its structural flexibility at each crystallographic site.[44–48] These NCS oxychalcogenides adopt the tetragonal crystal system with the space group of $P\bar{4}2_1m$ (no. 113), which displays alternating 2D $[MM'_2S_6]^{4-}$ layers with the charge-balanced AE^{2+} cations occupying the space between these layers. In this work, a new NCS melilite oxychalcogenide, $Sr_2FeGe_2OS_6$, has been prepared by an isomorphous substitution method. Excitingly, it is the first Fe-based example capable of achieving PM in the IR-NLO chalcogenide system, and displays an outstandingly comprehensive IR-NLO performance, including wide E_g (2.24 eV), sufficient d_{eff} (5.89 pm V^{-1}) and strong LIDT (14.42 MW cm^{-2}). Moreover, the relationships between the microscopic crystal structure and macroscopic NLO activity were systematically investigated.

Experimental section

Synthesis and characterization

The raw materials were purchased from Aladdin (SrO, AR; $FeCl_2$, 2.5N; Ge, 5N; S, 3.5N; Ba, 3N; KI, 4N) and stored in an Ar-filled glovebox. Single crystals of $Sr_2FeGe_2OS_6$ were grown by the flux method. A mixture of 2 mmol SrO (93 mg), 1 mmol $FeCl_2$ (57 mg), 2 mmol Ge (65 mg), 6 mmol S (86 mg), and 1 mmol Ba (38 mg) was weighed and an additional 300 mg of KI was added as the reactive flux. The mixture was placed in a 7 mm inner-diameter silica crucible and then in a vacuum-sealed silica tube with 11 mm inner-diameter. The samples were gradually heated to 673 K, held for 15 h, and then heated to 1073 K at a rate of 10 K h^{-1}, held for 3 days, and then slowly cooled to 623 K at a rate of 3 K h^{-1}. High-quality black-red block crystals (approximately 90% yield based on Fe) for single-crystal X-ray diffraction measurements were obtained after washing with 95% ethanol and being manually selected for characterization. Single-crystal X-ray diffraction (XRD) data for $Sr_2FeGe_2OS_6$ were collected at 100 K using a Rigaku Oxford Hybrid Pixel Array diffractometer by Ga K_α radiation (λ = 1.3405 Å). Semiquantitative microprobe analyses were performed *via* a field emission scanning electron microscope (JSM6700F, operating at 10 kV) equipped with an energy dispersive X-ray spectroscope (EDS, Oxford INCA). Thermogravimetry (TG) analysis was performed under a flowing N_2 atmosphere at 313–1273 K using a NETZSCH STA 449C simultaneous analyzer. X-ray photoelectron spectroscopy (XPS) spectra were recorded using ESCALAB 250Xi equipment with C 1s at 284.8 eV as the internal standard. Diffuse-reflectance spectra were recorded using a PerkinElmer LAMBDA 950 spectrophotometer at 200–2500 nm. The SHG and LIDT measurements using $AgGaS_2$ as the reference were implemented by the Kurtz–Perry method (2050 nm)[49] and the single pulse measurement method (1064 nm),[50] respectively. Theoretical investigations were also performed based on the density functional theory (DFT) method (refer to the ESI† for the detailed experimental section).

Results and discussion

Single-crystal XRD data for $Sr_2FeGe_2OS_6$ are well indexed to the tetragonal system (space group $P\bar{4}2_1m$ (no. 113)) and categorized into melilite structure type. There are one Sr, one Ge, one Fe, one O and two S crystallographically independent atoms in the unit cell (Table S1†). The crystallographic parameters and diagrammatic sketch of the structure can be found in Table 1 and Fig. 1, respectively. As shown in Fig. 1, $Sr_2FeGe_2OS_6$ features a 2D $\{[FeGe_2OS_6]\}^{4-}$ pentagonal tiling layer stacked in the same mode along the c axis with inserted Sr^{2+} to realize charge balance. In the structure of $Sr_2FeGe_2OS_6$, adjacent [$GeOS_3$] tetrahedra are linked with each other *via* corner-sharing O atoms and polymerize into [Ge_2OS_6] dimers. Two [FeS_4] units bridge with one [Ge_2OS_6] dimer and one [$GeOS_3$] tetrahedron by corner-sharing S atoms to form a pentagonal ring, which

Table 1 Crystallographic data and refinement details for $Sr_2FeGe_2OS_6$

Empirical formula	$Sr_2FeGe_2OS_6$
Formula weight	584.63
Temperature (K)	100(2)
Crystal system	Tetragonal
Space group	$P\bar{4}2_1m$ (no. 113)
a (Å)	9.4182(2)
b (Å)	9.4182(2)
c (Å)	6.1470(2)
V (Å^3)	545.25(3)
Z	2
D_c (g cm^{-3})	3.561
μ (mm^{-1})	26.599
GOOF on F^2	1.066
R_1, wR_2 ($I > 2\sigma(I)$)[a]	0.0217, 0.0519
R_1, wR_2 (all data)	0.0219, 0.0521
CCDC number	2227377
Largest diff. peak and hole (e Å^{-3})	1.092, −0.497

[a] $R_1 = \sum||F_o| - |F_c||/\sum|F_o|$, $wR_2 = [\sum w(F_o^2 - F_c^2)^2/\sum w(F_o^2)^2]^{1/2}$.

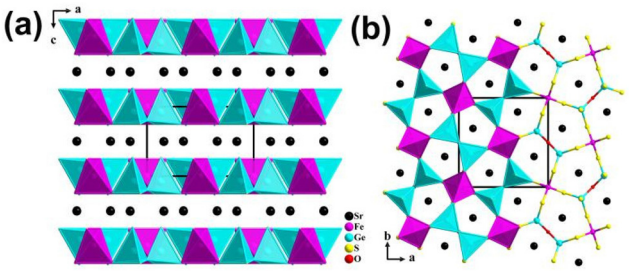

Fig. 1 Crystal structure of $Sr_2FeGe_2OS_6$: (a) schematic illustration of the structure along the *b* axis and (b) view along the *ab*-plane.

further interlinks to form a 2D $\{[FeGe_2OS_6]\}^{4-}$ layer with 6.1470 (2) Å layer spacing. The bond length in the $[FeS_4]$ tetrahedron is d_{Fe-S} = 2.3252 Å, which is similar to d_{Fe-S} values of 2.332 (3)–2.374 (4) Å in $K_2FeGe_3S_8$ [32] and 2.320 (1)–2.332 (1) Å in $K_{10}Fe_4Sn_4S_{17}$.[51] The detailed information about other important bond lengths and angles are described in Table S2 and Fig. S1.† Interestingly, we found that the M–S bond length may be negatively correlated with the electronegativity of M by comparing the local structures of the reported melilite oxychalcogenides $Sr_2MM'_2OS_6$ (M = Mn, Co, Zn, Cd; M′ = Ge, Sn) (Table S3†).[44–48]

The black-red block crystals of $Sr_2FeGe_2OS_6$ were obtained with a high yield through the flux method at 1123 K. The experimental powder XRD pattern is consistent with the simulated one (Fig. 2a), indicating that high phase purity of the title compound can be obtained according to the aforementioned synthesis process. XPS measurements were accomplished to elucidate the oxidation state of Fe ions. Fig. 2b shows the Fe 2p core levels of XPS narrow-scan spectra and Fig. S2† reveals the XPS data of other elements in $Sr_2FeGe_2OS_6$. As shown in Fig. 2b, there are two peaks in the Fe 2p core level spectra, which can be assigned to Fe $2p_{1/2}$ and Fe $2p_{3/2}$. These two signals are similar to those of Fe^{2+} in FeO[52] and Fe_2SiO_4,[53] indicating that the oxidation states of the Fe ions are +2. These results show that the precise formula of the ionic valence state is $(Sr^{2+})_2(Fe^{2+})(Ge^{4+})_2(O^{2-})(S^{2-})_6$. Moreover, the uniform distribution and atomic ratio of Sr/Fe/Ge/O/S = 1.9/1/1.9/1/6.2 approximate with the target value and were determined as shown in the results of SEM and EDS mapping analyses (Fig. S3†). The distribution of O beyond the crystal was probably affected by the O-containing conductive substrate and its light atomic weight compared with other elements. The TG analysis curves indicated that $Sr_2FeGe_2OS_6$ has good thermal stability up to 1071 K under an N_2 atmosphere (Fig. 2c) but starts to decompose with apparent weight loss at higher temperatures. This is in accordance with the results of powder XRD analysis and impurities of $SrGeO_3$ and $Fe_{0.96}S$ were detected (as shown in Fig. S4†). As depicted in the room-temperature UV-vis absorption spectra (Fig. 2d), the deduced E_g of $Sr_2FeGe_2OS_6$ is 2.24 eV using the equation for an indirect bandgap semiconductor,[54] which corresponds to its black-red crystal color (the inset picture in Fig. 2d). We compared the E_g value with those of typical Fe-containing materials[31,32,51–63] according to a detailed literature survey, as shown in Fig. 2e, and found that $Sr_2FeGe_2OS_6$ displays the largest E_g among the 16 reported compounds based on experimental measurements. This phenomenon also illustrates that oxychalcogenides as IR-NLO candidates have advantage in the E_g compared with sulfides. Besides, the wide E_g is comparable to those of commercial IR-NLO materials $AgGaS_2$ (2.56 eV),[64] $AgGaSe_2$ (1.83 eV)[65] and $ZnGeP_2$ (2.0 eV).[66] However, this value is narrower than those of the 7 existing melilite materials $AE_2MM'_2OS_6$ (Table S3†),[44–48] *e.g.*, 2.77–3.73 eV, which can be attributed to the strong optical absorption in the UV-vis region caused by the d–d charge transitions of d^6 Fe^{2+}.[32,51]

In general, the NCS structure is the paramount precondition for IR-NLO materials. The SHG signals of the target material were assessed *via* the Kurtz–Perry method[49] with 2050 nm irradiation (10 mJ). As depicted in Fig. 3(a), the SHG intensities present an upward trend with increasing particle size and then approach saturation, which reveals that $Sr_2FeGe_2OS_6$ possesses good PM nature. As far as we know, it is the first example of Fe-based compounds that has typical type-I PM behaviour. Significantly, this good PM behaviour is one of the preliminary requirements in being able to realize IR-NLO application. Moreover, the relative SHG efficiency of the title compound was compared with that of a sample of the typical commercial IR-NLO material $AgGaS_2$. As shown in Fig. 3(b), $Sr_2FeGe_2OS_6$ exhibits a moderate SHG response, which is almost 0.5 times as large as that of the reference in the particle size range of 150–210 μm. Its SHG efficiency ranks among the middle of the reported melilite materials $AE_2MM'_2OS_6$ (d_{eff} = 0.3–2.1 × $AgGaS_2$, see Table S3† for details)[44–48] and is comparable with other d-block metal-containing oxychalcogenides, such as $RE_3NbS_3O_4$ (RE = Sm, Gd; d_{eff} = 0.3–0.4 × $AgGaS_2$),[67] $Sr_4Pb_{1.5}Sb_5O_5Se_8$ (d_{eff} = 0.25 × $AgGaS_2$),[68] $AEGeOS_2$ (AE = Sr, Ba; d_{eff} = 0.4–0.5 × $AgGaS_2$),[69] and $Ba_2SnSi_2SO_7$ (d_{eff} = 0.6 × $AgGaS_2$).[70] The powder LIDT of $Sr_2FeGe_2OS_6$ has also been tested as another important index to evaluate its NLO performance *via* the particle size range of

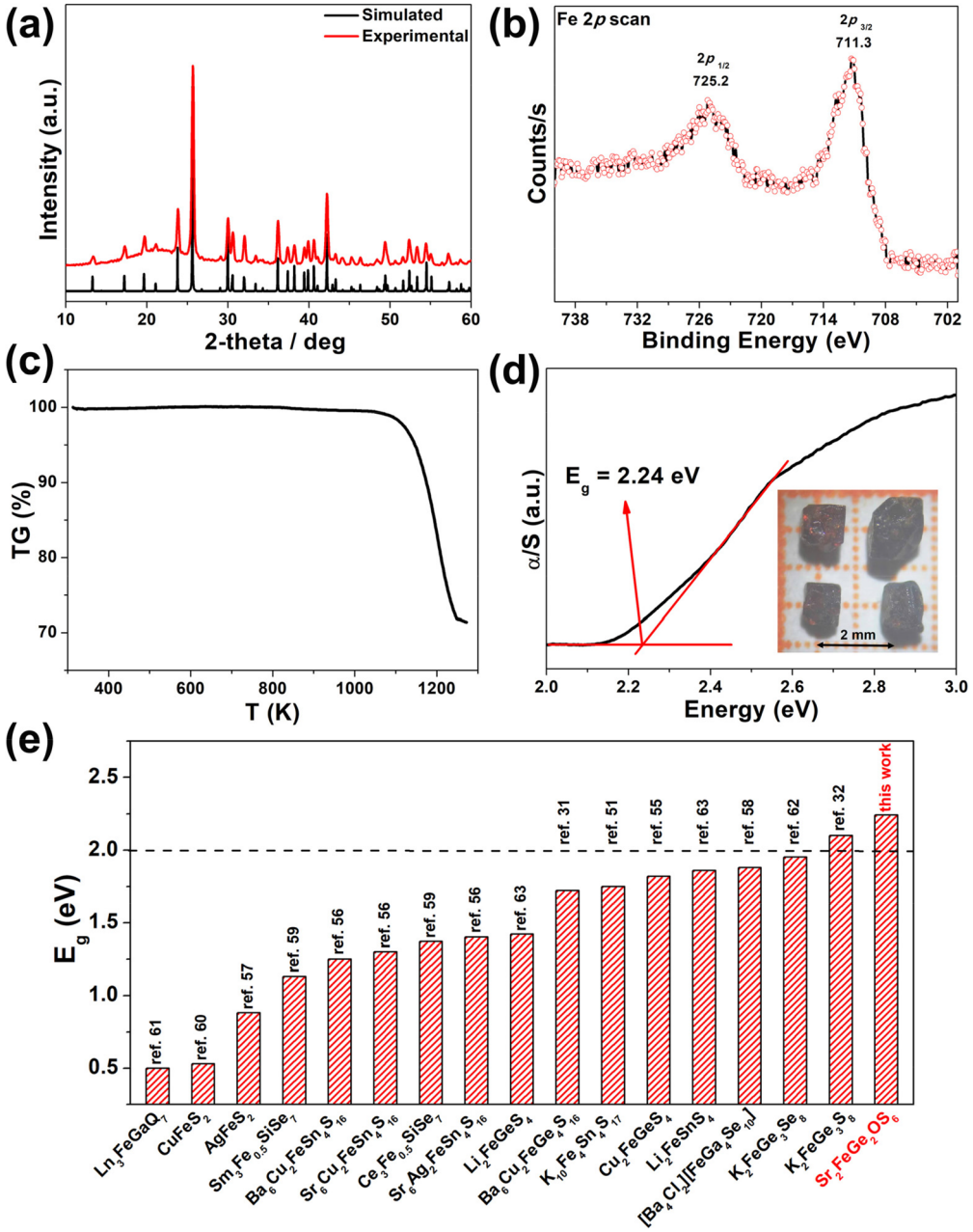

Fig. 2 Experimental results of $Sr_2FeGe_2OS_6$. (a) the XRD patterns; (b) Fe 2p narrow-scan XPS spectra; (c) TG diagram; (d) diffuse-reflectance spectrum; the inset shows a photograph of the crystals; and (e) comparison of the experimental E_g of $Sr_2FeGe_2OS_6$ with E_g values of typical Fe-based chalcogenides.

150–210 μm under a 1064 nm laser and the experimental result is about 14.42 MW cm^{-2}. It is clear that the LIDT of the title compound is significantly larger by 5 times that of $AgGaS_2$, indicating its positive thermal conduction capability. Owing to the LIDT being generally consistent with the value of E_g, the title compound has a relatively smaller LIDT than most other melilite materials $AE_2MM'_2OS_6$ (Table S3†) (*e.g.*, LIDT = 6–21 × $AgGaS_2$),[44–48] but excellent heat tolerance among the reported Fe-based materials can be speculated.

Systematic theoretical calculations based on DFT as an effective means to discover the structure–activity relationship have been analysed in detail. The results displayed in Fig. 4a suggest an indirect semiconducting state with a calculated E_g of 1.94 eV for $Sr_2FeGe_2OS_6$ along the *Q*–*Z* direction between the highest valence band (VB) and the lowest conduction band (CB). This relatively smaller value compared with the experimental value (E_g = 2.24 eV) is mainly ascribed to the common problem of DFT calculation.[71–73] Besides, the first Brillouin zone with high symmetry points of the title compound is provided in Fig. S5.† The Perdew–Burke–Ernzerhof (PBE) approach[74] was used to calculate the partial densities of states (PDOS) of $Sr_2FeGe_2OS_6$ (Fig. 4b). From −10 eV to the Fermi

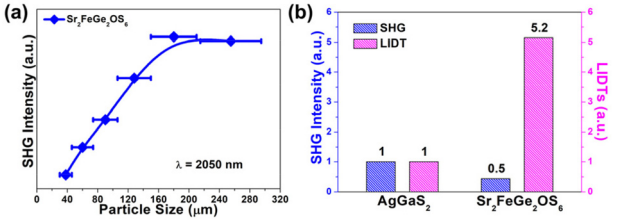

Fig. 3 (a) SHG responses of $Sr_2FeGe_2OS_6$ *versus* particle size under a 2050 nm incident laser and (b) results of the SHG and LIDT intensities of $Sr_2FeGe_2OS_6$ and $AgGaS_2$ powders with the largest particle-size range of 150–210 μm.

level (E_F = 0 eV), S 3p, Fe 3d, O 2p, and Ge 4s orbitals make a major contribution and the Fe 3d, S 3p, Ge 4p, and Ge 4s orbitals contribute mostly in the energy field ranging from 0 eV to +10 eV. Therefore, it can be deduced that the charge transitions responsible for the optical E_g absorption could be determined by [$GeOS_3$] and [FeS_4] BBUs, *i.e.*, the 2D $\{[FeGe_2OS_6]^{4-}\}_n$ layered structure.

Space group $P\bar{4}2_1m$ of $Sr_2FeGe_2OS_6$ belongs to the asymmetrical point group of 2*m*, and thus, only has one non-vanishing independent SHG coefficient d_{14} under the constraint of Kleinman symmetry.[75] The calculated frequency-dependent SHG coefficient d_{14} at 2050 nm (*ca.* 0.61 eV) is 11.79 pm V^{-1} (the upper panel of Fig. 4c), which is slightly larger than the experimental result (Fig. 3b). The absorption of output frequency-doubled light at 1025 nm was possibly the main reason. As plotted in the lower panel of Fig. 4c, the calculated birefringence Δn ($\Delta n = n_z - n_x$) value was 0.127 at 2050 nm, which is obviously greater than that of $AgGaS_2$ (Δn = 0.04) under the same conditions.[76–78] Besides, such a large Δn exceeds that of the melilite structure type $Sr_2MGe_2OS_6$ (M = Co, Mn, Zn; Δn = 0.064–0.124),[44–46,48] indicating that $Sr_2FeGe_2OS_6$ can theoretically realize PM in the IR region. Moreover, the minimum PM cut-off wavelengths on the basis of the refractive-index dispersion curves were calculated using the formula $n_x(2w) = n_z(w)$.[79–82] As shown in Fig. 4d, the shortest cut-off edge of SHG light was evaluated to be 600 nm under the restriction of type-I PM conditions.

In order to determine which microscopic NLO active units provide the most forceful contribution to the macroscopic NLO performance from the view of the micro-structure, we reveal a cutoff-energy-dependent SHG coefficient (Fig. 5a) accompanied by partial-charge-density maps (Fig. 5b) in terms of the so-called length-gauge formalism.[83] From the calculation results presented in Fig. 5, the remarkable increase of d_{14} in the VB-1, CB-1, and CB-3 intervals can be directly observed, indicating

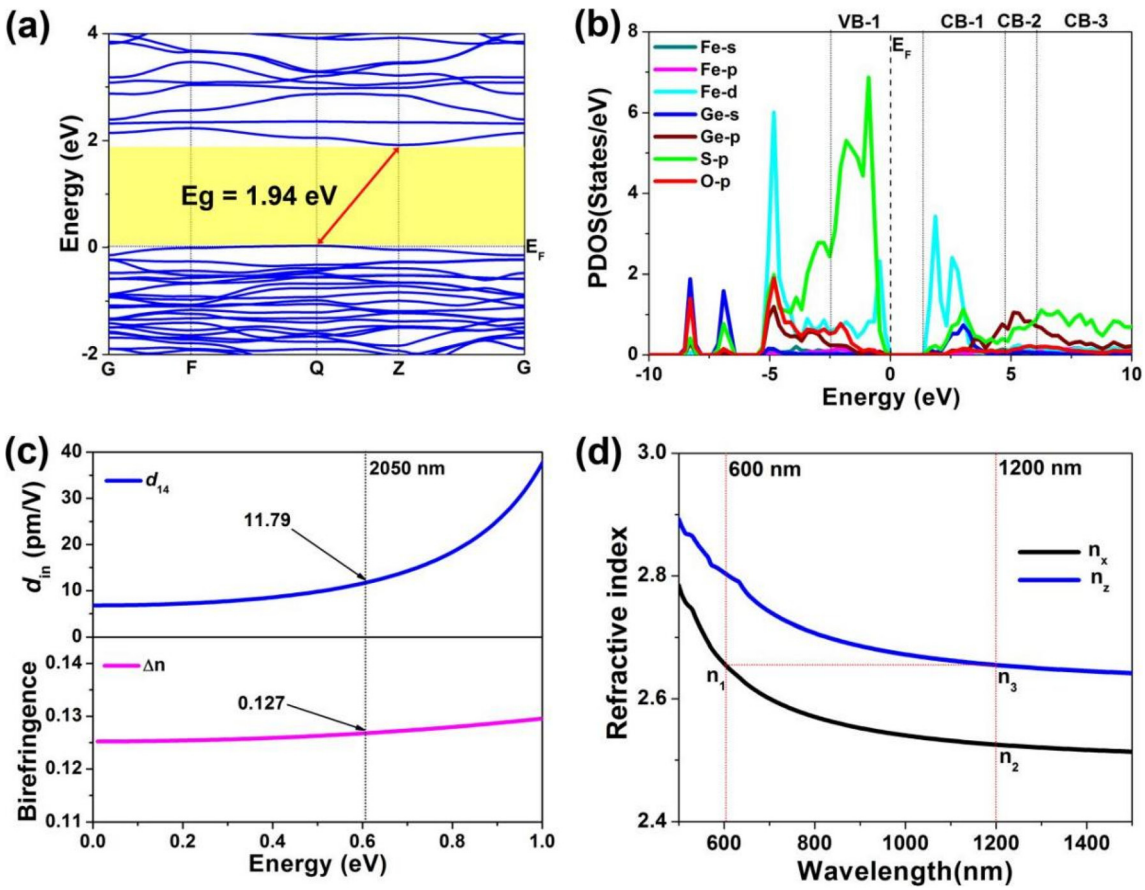

Fig. 4 Theoretical calculation results of (a) the band structure; (b) PDOS; (c) energy (eV) dependence of the static d_{14} (pm V^{-1}) (the top panel) and birefringence at 2050 nm (the bottom panel); and (d) dispersion of the refractive indices.

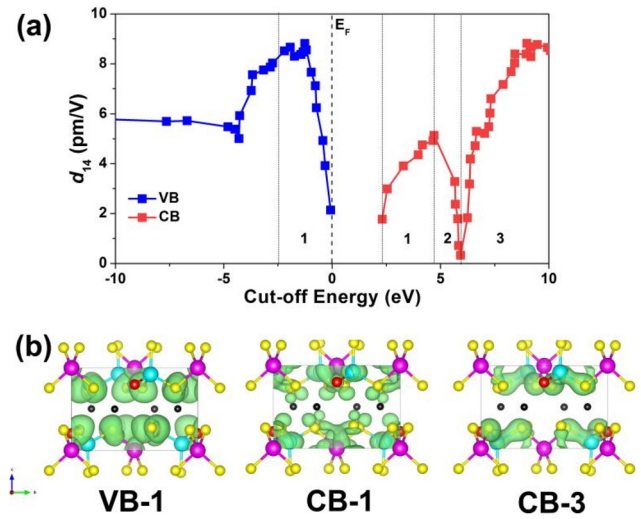

Fig. 5 (a) Variation of static coefficient d_{14} along with cut-off energy (eV). (b) Projection of the partial charge density maps in the VB-1, CB-1 and CB-3 intervals.

that these energy ranges contribute significantly to the SHG intensity. In accordance with the associated PDOS (Fig. 4b), the VB-1 region is dominated by S 3p, Fe 3d, and O 2p states, the CB-1 region mainly consists of Fe 3d, S 3p, and Ge 4s states, while S 3p and Ge 4p states produce the major contribution to the CB-3 region. Consequently, the strong SHG response for $Sr_2FeGe_2OS_6$ can be assigned to the $[GeOS_3]$ and $[FeS_4]$ BBUs, which are the source of increased SHG efficiency.

Conclusions

In summary, a new NCS melilite oxychalcogenide, $Sr_2FeGe_2OS_6$, was successfully designed and prepared through an isomorphous substitution strategy. $Sr_2FeGe_2OS_6$ features a 2D $\{[FeGe_2OS_6]^{4-}\}_n$ layered structure formed by corner-sharing $[Ge_2OS_6]$ dimers and $[FeS_4]$ tetrahedra with Sr^{2+} embedded in these layers. Experimental results from a powder sample of $Sr_2FeGe_2OS_6$ indicate that it possesses a wide E_g (2.24 eV), sufficient d_{eff} (*ca.* 0.5 × $AgGaS_2$) and strong LIDT (*ca.* 5.2 × $AgGaS_2$). Detailed theoretical investigations illustrate that the unique arrangement of NLO-active motifs, $[Ge_2OS_6]$ dimers and $[FeS_4]$ tetrahedra, mainly contributes to the strong d_{eff} and large Δn of $Sr_2FeGe_2OS_6$. Furthermore, $Sr_2FeGe_2OS_6$ is the first PM Fe-based IR-NLO example to be realized by isomorphous substitution. These findings not only broaden the horizon of the NCS transition-metal-based chalcogenide system, but also provide a feasible strategy to discover high-performance IR-NLO candidates.

Author contributions

H. D. Yang prepared the samples, designed and carried out the experiments, and wrote the manuscript. S. H. Zhou carried out the theoretical calculations. M. Y. Ran helped solve the structure of the title compound. X. T. Wu put forward suggestions about the structure–property relationship. H. Lin and Q. L. Zhu analyzed the results and edited the manuscript. All the authors have approved the final version of the manuscript. H. D. Yang and S. H. Zhou contributed equally to this work.

Conflicts of interest

There are no conflicts to declare.

Acknowledgements

This research was supported by the National Natural Science Foundation of China (22175175, 22193043), the Fujian Science and Technology Innovation Laboratory for Optoelectronic Information of China (2021ZR118), and the Natural Science Foundation of Fujian Province (2022L3092) and the Youth Innovation Promotion Association CAS (2022303). We thank Professor Bing-Xuan Li at FJIRSM for helping with the NLO measurements and Professor Yong-Fan Zhang at Fuzhou University for helping with DFT calculations.

References

1 V. Petrov, Frequency down-conversion of solid-state laser sources to the mid-infrared spectral range using non-oxide nonlinear crystals, *Prog. Quantum Electron.*, 2015, **42**, 1–106.
2 *Structure-Property Relationships in Nonlinear Optical Crystals II The IR Region*, ed. X.-T. Wu and L. Chen, Structure and Bonding, Series ed. D. M. Mingos, Springer, New York, 2012, p. 145.
3 V. A. Serebryakov, E. V. Boiko, N. N. Petrishchev and A. V. Yan, Medical applications of mid-TR lasers: problems and prospects., *J. Opt. Technol.*, 2010, 77, 6–17.
4 F. J. Duarte, *Tunable Laser Applications*, CRC Press, Boca Raton, FL, 2nd edn, 2008, ch. 2, 9, and 12.
5 D. N. Nikogosyan, *Nonlinear Optical Crystals: A Complete Survey*, Springer-Science, New York, 2005.
6 Y. Li, J. Luo and S. Zhao, Local Polarity-Induced Assembly of Second-Order Nonlinear Optical Materials, *Acc. Chem. Res.*, 2022, **55**, 3460–3469.
7 U. Keller, Recent developments in compact ultrafast lasers, *Nature*, 2003, **424**, 831–838.
8 A. Harasaki and K. Kato, New Data on the Nonlinear Optical Constant, Phase-Matching, and Optical Damage of AgGaS2, *Jpn. J. Appl. Phys*, 1997, **36**, 700–703.
9 G. D. Boyd, E. Buehler and F. G. Storz, Linear and nonlinear optical properties of $ZnGeP_2$ and CdSe, *Appl. Phys. Lett.*, 1971, **18**, 301–304.
10 G. C. Catella, L. R. Shiozawa, J. R. Hietanen, R. C. Eckardt, R. K. Route, R. S. Feigelson, D. G. Cooper and C. L. Marquardt, Mid-IR absorption in AgGaSe2 optical

parametric oscillator crystals, *Appl. Opt.*, 1993, **32**, 3948–3951.

11 M.-Y. Ran, A.-Y. Wang, W.-B. Wei, X.-T. Wu, H. Lin and Q.-L. Zhu, Recent progress in the design of IR nonlinear optical materials by partial chemical substitution: structural evolution and performance, *Coord. Chem. Rev.*, 2023, **484**, 215059.

12 F. Liang, L. Kang, Z. Lin, Y. Wu and C. Chen, Analysis and prediction of mid-IR nonlinear optical metal sulfides with diamond-like structures, *Coord. Chem. Rev.*, 2017, **333**, 57–70.

13 S.-P. Guo, Y. Chi and G.-C. Guo, Recent achievements on middle and far-infrared second-order nonlinear optical materials, *Coord. Chem. Rev.*, 2017, **335**, 44–57.

14 P. S. Halasyamani, Asymmetric Cation Coordination in Oxide Materials: Influence of Lone-Pair Cations on the Intra-octahedral Distortion in d0 Transition Metals, *Chem. Mater.*, 2004, **16**, 3586–3592.

15 H. Chen, W.-B. Wei, H. Lin and X.-T. Wu, Transition-metal-based chalcogenides: A rich source of infrared nonlinear optical materials, *Coord. Chem. Rev.*, 2021, **448**, 214154.

16 G. Li, Z. Yang, J. Li and S. Pan, A review of the $A^{I}{}_{2}B^{II}C^{IV}D^{VI}{}_{4}$ family as infrared nonlinear optical materials: the effect of each site on the structure and optical properties, *Chem. Commun.*, 2020, **56**, 11565–11576.

17 H. Chen, M.-Y. Ran, W.-B. Wei, X.-T. Wu, H. Lin and Q.-L. Zhu, A comprehensive review on metal chalcogenides with three-dimensional frameworks for infrared nonlinear optical applications, *Coord. Chem. Rev.*, 2022, **470**, 214706.

18 J. Guillevic, L. Jy and D. Grandjean, Etude Structurale de Combinaisons Sulfurees et Seleniees du Molybdene. IV. Structures Cristallines de $CoMo_2S_4$ et de $FeMo_2S_4$, *Acta Crystallogr., Sect. B: Struct. Crystallogr. Cryst. Chem.*, 1974, **30**, 111–117.

19 K. Sato and T. Teranishi, Optical Absorption Spectrum of a Thin $CuFeS_2$ Film, *J. Phys. Soc. Jpn.*, 1976, **40**, 297–298.

20 J. M. D. Coey, E. Devlin and R. J. Gambino, Noncrystalline ferromagnetic irongallium oxide, *J. Appl. Phys.*, 1982, **53**, 7810–7812.

21 Y.-H. Chu, L. W. Martin, M. B. Holcomb and R. Ramesh, Controlling magnetism with multiferroics, *Mater. Today*, 2007, **10**, 16–23.

22 K. Kovnir, V. O. Garlea, C. M. Thompson, H. D. Zhou, W. M. Reiff, A. Ozarowski and M. Shatruk, Spin-Glass Behavior in $LaFe_xCo_{2-x}P_2$ Solid Solutions: Interplay Between Magnetic Properties and Crystal and Electronic Structures, *Inorg. Chem.*, 2011, **50**, 10274–10283.

23 W. Jeitschko, U. Meisen and J. Albering, Actinoid transition metal phosphides $An_2T_{12}P_7$ (An = Th, U; T = Fe, Co, Ni) and arsenides $An_2T_{12}As_7$ (An = Th, U; T = Co, Ni) with $Zr_2Fe_{12}P_7$ type structure, *Dalton Trans.*, 2010, **39**, 6067–6073.

24 O. Yakubovich, V. Urusov, W. Massa, G. Frenzen and D. Babel, Structure of $Na_2Fe_2F_7$ and Structural Relations in the Family of Weberites $Na_2M^{II}M^{III}F_7$, *Z. Anorg. Allg. Chem.*, 1993, **619**, 1909–1919.

25 G. Courbion, C. Jacoboni and R. Depape, The Dimorphism of $LiMnFeF_6$: A New Kind of Cationic Order in the Structural Type Na_2SiF_6, *J. Solid State Chem.*, 1982, **45**, 127–134.

26 E. Parthe and S. Z. Hu, $CaFeO_2Cl$ and Ca_2FeO_3Cl with higher space group ymmetry, a reevaluation, *J. Solid State Chem.*, 2003, **174**, 165–166.

27 K. Tustain, L. Farrar, W. Yao, P. Lightfoot, I. da Silva, M. T. F. Telling and L. Clark, Materialization of a Geometrically Frustrated Magnet in a Hybrid Coordination Framework: A Study of the Iron(II) Oxalate Fluoride Framework, $KFe(C_2O_4)F$, *Inorg. Chem.*, 2019, **58**, 11971–11977.

28 H. D. Yang, M. Y. Ran, S. H. Zhou, X. T. Wu, H. Lin and Q. L. Zhu, Rational design via dual-site aliovalent substitution leads to an outstanding IR nonlinear optical material with well-balanced comprehensive properties, *Chem. Sci.*, 2022, **13**, 10725–10733.

29 S. Pascal, S. David, C. Andraud and O. Maury, Near-infrared dyes for two-photon absorption in the short-wavelength infrared: strategies towards optical power limiting, *Chem. Soc. Rev.*, 2021, **50**, 6613–6658.

30 Y. Wang and R. K. Li, $K_2Fe_2B_2O_7$: A transparent nonlinear optical crystal with frustrated magnetism, *J. Solid State Chem.*, 2010, **183**, 1221–1225.

31 W. Cao, D. Mei, Y. Yang, Y. Wu, L. Zhang, Y. Wu, X. He, Z. Lin and F. Huang, From $CuFeS_2$ to $Ba_6Cu_2FeGe_4S_{16}$: rational band gap engineering achieves large second-harmonic-generation together with high laser damage threshold, *Chem. Commun.*, 2019, **55**, 14510–14513.

32 B. Ji, K. Pandey, C. P. Harmer, F. Wang, K. Wu, J. Hu and J. Wang, Centrosymmetric or Noncentrosymmetric? Transition Metals Talking in $K_2TGe_3S_8$ (T = Co, Fe), *Inorg. Chem.*, 2021, **60**, 10603–10613.

33 Z. T. Messegee, J. S. Cho, A. J. Craig, V. O. Garlea, Y. Xin, C. J. Kang, T. E. Proffen, H. Bhandari, J. C. Kelly, N. J. Ghimire, J. A. Aitken, J. I. Jang and X. Tan, Multifunctional Cu_2TSiS_4 (T = Mn and Fe): Polar Semiconducting Antiferromagnets with Nonlinear Optical Properties, *Inorg. Chem.*, 2023, **62**, 530–542.

34 M. M. Chen, S. H. Zhou, W. B. Wei, X. T. Wu, H. Lin and Q. L. Zhu, Phase Matchability Transformation in the Infrared Nonlinear Optical Materials with Diamond–Like Frameworks, *Adv. Opt. Mater.*, 2022, **10**, 2102123.

35 H. Lin, L. Chen, J. S. Yu, H. Chen and L. M. Wu, Infrared SHG Materials CsM_3Se_6 (M = Ga/Sn, In/Sn): Phase Matchability Controlled by Dipole Moment of the Asymmetric Building Unit, *Chem. Mater.*, 2017, **29**, 499–503.

36 Y. X. Zhang, B. X. Li, H. Lin, Z. J. Ma, X. T. Wu and Q. L. Zhu, Impressive Second Harmonic Generation Response in a Novel Phase-Matchable NLO-active MOF Derived from Achiral Precursors, *J. Mater. Chem. C*, 2019, **7**, 6217–6221.

37 H. Chen, Y. Y. Li, B. X. Li, P. F. Liu, H. Lin, Q. L. Zhu and X. T. Wu, Salt-Inclusion Chalcogenide $[Ba_4Cl_2][ZnGa_4S_{10}]$: Rational Design of an IR Nonlinear Optical Material with Superior Comprehensive Performance Derived from AgGaS2, *Chem. Mater.*, 2020, **32**, 8012–8019.

38 H. Lin, W.-B. Wei, H. Chen, X.-T. Wu and Q.-L. Zhu, Rational design of infrared nonlinear optical chalcogenides by chemical substitution, *Coord. Chem. Rev.*, 2020, **406**, 213150.

39 M.-M. Chen, S.-H. Zhou, W. Wei, M.-Y. Ran, B. Li, X.-T. Wu, H. Lin and Q.-L. Zhu, $RbBiP_2S_6$: A Promising IR Nonlinear Optical Material with a Giant Second-Harmonic Generation Response Designed by Aliovalent Substitution, *ACS Mater. Lett.*, 2022, **4**, 1264–1269.

40 M. Y. Ran, Z. J. Ma, H. Chen, B. X. Li, X. T. Wu, H. Lin and Q. L. Zhu, Partial Isovalent Anion Substitution to Access Remarkable Second-Harmonic Generation Response: A Generic and Effective Strategy for Design of Infrared Nonlinear Optical Materials, *Chem. Mater.*, 2020, **32**, 5890–5896.

41 Y. F. Shi, W. B. Wei, X. T. Wu, H. Lin and Q. L. Zhu, Recent progress in oxychalcogenides as IR nonlinear optical materials, *Dalton Trans.*, 2021, **50**, 4112–4118.

42 Y. Zhang, H. Wu, Z. Hu and H. Yu, Oxychalcogenides: A Promising Materials Class for Nonlinear Optical Crystals with Mixed-anion Groups, *Chem. – Eur. J.*, 2022, e202203597.

43 M.-Y. Ran, S.-H. Zhou, W. Wei, B. Li, X.-T. Wu, H. Lin and Q.-L. Zhu, Rational Design of a Rare-Earth Oxychalcogenide $Nd_3[Ga_3O_3S_3][Ge_2O_7]$ with Superior Infrared Nonlinear Optical Performance, *Small*, 2023, **19**, 2300248.

44 M.-Y. Ran, S.-H. Zhou, B. Li, W. Wei, X.-T. Wu, H. Lin and Q.-L. Zhu, Enhanced Second-Harmonic-Generation Efficiency and Birefringence in Melilite Oxychalcogenides $Sr_2MGe_2OS_6$ (M = Mn, Zn, and Cd), *Chem. Mater.*, 2022, **34**, 3853–3861.

45 R. Wang, F. Liang, X. Liu, Y. Xiao, Q. Liu, X. Zhang, L. M. Wu, L. Chen and F. Huang, Heteroanionic Melilite Oxysulfide: A Promising Infrared Nonlinear Optical Candidate with a Strong Second-Harmonic Generation Response, Sufficient Birefringence, and Wide Bandgap, *ACS Appl. Mater. Interfaces*, 2022, **14**, 23645–23652.

46 X. Tian, X. Zhang, Y. Xiao, X. Wu, B. Zhang, D. Yang and K. Wu, From oxides to oxysulfides: the mixed-anion GeS_3O unit induces huge improvement in the nonlinear optical effect and optical anisotropy for potential nonlinear optical materials, *RSC Adv.*, 2022, **12**, 16296–16300.

47 Y. Cheng, H. Wu, H. Yu, Z. Hu, J. Wang and Y. Wu, Rational Design of a Promising Oxychalcogenide Infrared Nonlinear Optical Crystal, *Chem. Sci.*, 2022, **13**, 5305–5310.

48 N. Zhang, Q. T. Xu, Z. H. Shi, M. Yang and S. P. Guo, Characterizations and Nonlinear-Optical Properties of Pentanary Transition-Metal Oxysulfide $Sr_2CoGe_2OS_6$, *Inorg. Chem.*, 2022, **61**, 17002–17006.

49 S. K. Kurtz and T. T. Perry, A Powder Technique for the Evaluation of Nonlinear Optical Materials, *J. Appl. Phys.*, 1968, **39**, 3798–3813.

50 M.-J. Zhang, X.-M. Jiang, L.-J. Zhou and G.-C. Guo, Two phases of Ga_2S_3: promising infrared second-order nonlinear optical materials with very high laser induced damage thresholds, *J. Mater. Chem. C*, 2013, **1**, 4754–4760.

51 O. Palchik, R. G. Iyer, C. G. Canlas, D. P. Weliky and M. G. Kanatzidis, $K_{10}M_4M'_4S_{17}$ (M = Mn, Fe, Co, Zn; M′ = Sn, Ge) and Cs10Cd4Sn4S17: Compounds with a Discrete Supertetrahedral Cluster, *Z. Anorg. Allg. Chem.*, 2004, **630**, 2237–2247.

52 P. S. Bagus, C. J. Nelin, C. R. Brundle, B. V. Crist, N. Lahiri and K. M. Rosso, Combined multiplet theory and experiment for the Fe 2p and 3p XPS of FeO and Fe_2O_3, *J. Chem. Phys.*, 2021, **154**, 094709.

53 T. Yamashita and P. Hayes, Analysis of XPS spectra of Fe^{2+} and Fe^{3+} ions in oxide materials, *Appl. Surf. Sci.*, 2008, **254**, 2441–2449.

54 M. A. Butler, Photoelectrolysis and physical properties of the semiconducting electrode WO_2, *J. Appl. Phys.*, 1977, **48**, 1914–1920.

55 M. Beraich, H. Shaili, E. Benhsina, Z. Hafidi, S. Mansouri, M. Taibi, F. Bentiss, A. Guenbour, A. Bellaouchou, A. Mzerd, A. Zarrouk and M. Fahoume, Preparation and characterization of Cu_2FeGeS_4 thin-film synthesized via spray ultrasonic method–DFT study, *Mater. Lett.*, 2020, **275**, 128070.

56 L. Zhang, D. Mei, Y. Wu, C. Shen, W. Hu, L. Zhang, J. Li, Y. Wu and X. He, Syntheses, structures, optical properties, and electronic structures of $Ba_6Cu_2GSn_4S_{16}$ (G = Fe, Ni) and $Sr_6D_2FeSn_4S_{16}$ (D = Cu, Ag), *J. Solid State Chem.*, 2019, **272**, 69–77.

57 X. Zheng, B. Sciacca, E. C. Garnett and L. Zhang, $AgFeS_2$-Nanowire-Modified $BiVO_4$ Photoanodes for Photoelectrochemical Water Splitting, *ChemPlusChem*, 2016, **81**, 1075–1082.

58 Y.-Y. Li, P.-F. Liu, L. Hu, L. Chen, H. Lin, L.-J. Zhou and L.-M. Wu, Strong IR NLO Material $Ba_4MGa_4Se_{10}Cl_2$: Highly Improved Laser Damage Threshold via Dual Ion Substitution Synergy, *Adv. Opt. Mater.*, 2015, **3**, 957–966.

59 J. He, Z. Wang, X. Zhang, Y. Cheng, Y. Gong, X. Lai, C. Zheng, J. Lin and F. Huang, Synthesis, structure, magnetic and photoelectric properties of $Ln_3M_{0.5}M'Se_7$ (Ln = La, Ce, Sm; M = Fe, Mn; M′ = Si, Ge) and $La_3MnGaSe_7$, *RSC Adv.*, 2015, **5**, 52629–52635.

60 Y. Li, T. Zhang, Y. Qin, T. Day, G. Jeffrey Snyder, X. Shi and L. Chen, Thermoelectric transport properties of diamond-like $Cu_{1-x}Fe_{1+x}S_2$ tetrahedral compounds, *J. Appl. Phys.*, 2014, **116**, 203705.

61 W. Yin, W. Wang, L. Kang, Z. Lin, K. Feng, Y. Shi, W. Hao, J. Yao and Y. Wu, Ln_3FeGaQ_7: A new series of transition-metal rare-earth chalcogenides, *J. Solid State Chem.*, 2013, **202**, 269–275.

62 K. Feng, W. Wang, R. He, L. Kang, W. Yin, Z. Lin, J. Yao, Y. Shi and Y. Wu, $K_2FeGe_3Se_8$: a new antiferromagnetic iron selenide, *Inorg. Chem.*, 2013, **52**, 2022–2028.

63 J. A. Brant, C. dela Cruz, J. Yao, A. P. Douvalis, T. Bakas, M. Sorescu and J. A. Aitken, Field-Induced Spin-Flop in Antiferromagnetic Semiconductors with Commensurate and Incommensurate Magnetic Structures: Li_2FeGeS_4 (LIGS) and Li_2FeSnS_4 (LITS), *Inorg. Chem.*, 2014, **53**, 12265–12274.

64 H. Lin, L. Chen, L. J. Zhou and L. M. Wu, Functionalization based on the substitutional flexibility: strong middle IR nonlinear optical selenides $AX^{II}_4X^{III}_5Se_{12}$, *J. Am. Chem. Soc.*, 2013, **135**, 12914–12921.

65 M. C. Ohmer and R. Pandey, Emergence of Chalcopyrites as Nonlinear Optical Materials, *MRS Bull.*, 1998, **23**, 16–22.

66 L. Bai, Z. Lin, Z. Wang, C. Chen and M. H. Lee, Mechanism of linear and nonlinear optical effects of chalcopyrite $AgGaX_2$ (X=S, Se, and Te) crystals, *J. Chem. Phys.*, 2004, **120**, 8772–8778.

67 X. Lian, Z. T. Lu, W. D. Yao, S. H. Yang, W. Liu, R. L. Tang and S. P. Guo, Structural Transformation and Second-Harmonic-Generation Activity in Rare-Earth and d0 Transition-Metal Oxysulfides $RE_3NbS_3O_4$ (RE = Ce, Sm, Gd, Dy), *Inorg. Chem.*, 2021, **60**, 10885–10889.

68 Y. Wang, M. Luo, P. Zhao, X. Che, Y. Cao and F. Huang, $Sr_4Pb_{1.5}Sb_5O_5Se_8$: a new mid-infrared nonlinear optical material with a moderate SHG response, *CrystEngComm*, 2020, **22**, 3526–3530.

69 X. Zhang, Y. Xiao, R. Wang, P. Fu, C. Zheng and F. Huang, Synthesis, crystal structures and optical properties of non-centrosymmetric oxysulfides $AeGeS_2O$ (Ae = Sr, Ba), *Dalton Trans.*, 2019, **48**, 14662–14668.

70 Y.-F. Shi, Z. Ma, B.-X. Li, X. Wu, H. Lin and Q.-L. Zhu, Phase matching achieved by isomorphous substitution in IR nonlinear optical material $Ba_2SnSSi_2O_7$ with an undiscovered $[SnO_4S]$ functional motif, *Mater. Chem. Front.*, 2022, **6**, 3054–3061.

71 K. Burke, Perspective on density functional theory, *J. Chem. Phys.*, 2012, **136**, 150901.

72 K. Govaerts, R. Saniz, B. Partoens and D. Lamoen, van der Waals bonding and the quasiparticle band structure of SnO from first principles, *Phys. Rev. B: Condens. Matter Mater. Phys.*, 2013, **87**, 235210.

73 N. E. Christensen, A. Svane and E. L. Peltzer y Blancá, Electronic and structural properties of SnO under pressure, *Phys. Rev. B: Condens. Matter Mater. Phys.*, 2005, **72**, 014109.

74 J. P. Perdew, K. Burke and M. Ernzerhof, Generalized Gradient Approximation Made Simple, *Phys. Rev. Lett.*, 1996, **77**, 3865–3868.

75 D. A. Kleinman, Nonlinear Dielectric Polarization in Optical Media, *Phys. Rev.*, 1962, **126**, 1977–1979.

76 M. Y. Li, B. X. Li, H. Lin, Z. J. Ma, L. M. Wu, X. T. Wu and Q. L. Zhu, $Sn_2Ga_2S_5$: A Polar Semiconductor with Exceptional Infrared Nonlinear Optical Properties Originating from the Combined Effect of Mixed Asymmetric Building Motifs, *Chem. Mater.*, 2019, **31**, 6268–6275.

77 C. Liu, S.-H. Zhou, Y. Xiao, C. Zhang, H. Lin and Y. Liu, Aliovalent-cation-substitution-induced structure transformation: a new path toward high-performance IR nonlinear optical materials, *J. Mater. Chem. C*, 2021, **9**, 15407–15414.

78 M.-Y. Ran, Z. Ma, X.-T. Wu, H. Lin and Q.-L. Zhu, $Ba_2Ge_2Te_5$: a ternary NLO-active telluride with unusual one-dimensional helical chains and giant second-harmonic-generation tensors, *Inorg. Chem. Front.*, 2021, **8**, 4838–4845.

79 H. Lin, Y. Y. Li, M. Y. Li, Z. J. Ma, L. M. Wu, X. T. Wu and Q. L. Zhu, Centric-to-acentric structure transformation induced by a stereochemically active lone pair: a new insight for design of IR nonlinear optical materials, *J. Mater. Chem. C*, 2019, **7**, 4638–4643.

80 M. Y. Li, Z. J. Ma, B. X. Li, X. T. Wu, H. Lin and Q. L. Zhu, $HgCuPS_4$: An Exceptional Infrared Nonlinear Optical Material with Defect Diamond-like Structure, *Chem. Mater.*, 2020, **32**, 4331–4339.

81 M.-M. Chen, Z. Ma, B.-X. Li, W.-B. Wei, X.-T. Wu, H. Lin and Q.-L. Zhu, $M_2As_2Q_5$ (M = Ba, Pb; Q = S, Se): A source of infrared nonlinear optical materials with excellent overall performance activated by multiple discrete arsenate anions, *J. Mater. Chem. C*, 2021, **9**, 1156–1163.

82 Y. Xiao, M. M. Chen, Y. Y. Shen, P. F. Liu, H. Lin and Y. Liu, $A_3Mn_2Sb_3S_8$ (A = K, Rb): A new type of multifunctional infrared nonlinear optical materials based on unique three-dimensional open frameworks, *Inorg. Chem. Front.*, 2021, **8**, 2835–2843.

83 C. Aversa and J. E. Sipe, Nonlinear optical susceptibilities of semiconductors: Results with a length-gauge analysis, *Phys. Rev. B: Condens. Matter Mater. Phys.*, 1995, **52**, 14636–14645.

